Vilnius University

Faculty of Physics

Ričardas Petkus

DEVELOPMENT OF SENSORS BASED ON FIELD-EFFECT TRANSISTORS AND INVESTIGATION OF THEIR OPTICAL CHARACTERISTICS AT 2.52 THZ

Master's thesis

Electronics and Telecommunications Technologies programme

Student	Ričardas Petkus
Approved	2026-05-22
Academic supervisor	dr. Dovilė Čibiraitė-Lukenskienė
Director of the Institute	dr. Robertas Grigalaitis

Vilnius 2026

TABLE OF CONTENTS

INTRODUCTION

Terahertz (THz) radiation is typically defined as the electromagnetic spectrum spanning from 0.1 THz to 10 THz [1]. The range in question falls between the high-frequency limit of conventional electronic devices and the low-frequency threshold of optical devices. The term 'terahertz gap' has been used to describe the difference between this region and its neighbours, as it is significantly less developed. The fundamental issue is that conventional semiconductor electronic devices, such as transistors, reach their frequency limits due to carrier transit times, whereas optical devices, such as semiconductor lasers, often require cryogenic cooling to overcome extremely low photon energies [2]. Despite these challenges, THz waves are in high interest in research due to their ability to penetrate non-conductive materials, their non-ionizing nature, and their specific resonance with the rotational and vibrational modes of complex biomolecules.

The paper focuses on a THz detector that utilises field-effect transistors (FETs). This technology is seamlessly compatible with model CMOS manufacturing processes as well as a desirable ability to operate efficiently at room temperature. Conventional electronics are based on high speed carrier transport, but THz FETs (TeraFETs) utilize the nonlinear properties of carrier density waves within the two-dimensional electron gas of the transistor channel [3]. This allows for the rectification of THz signals even when the radiation frequency far exceeds the device's own cutoff frequency. These FET-based sensors are particularly advantageous for the development of detector matrices, offering the high speed and scalability required for real-time imaging with continuous-wave sources.

The materials and tools for this work were supplied by Optoelectronic Systems Characterisation Laboratory and Terahertz Photonics Laboratory of Center for Physical Sciences and Technology (FTMC) and Laboratory of THz Electronics and Fluctuations of Vilnius University Faculty of Physics.

The aim of this work is to develop terahertz sensors based on TeraFET technology and to study their angular characteristic while working in 2.52 THz frequency in order to add to the laboratory's existing research foundation. Since the modelling above 1 THz is computationally intensive and often inaccurate, the experimental measurements are crucial for the verification and refinement of the required results. The study's initial phase is focused on the preparation of the experimental setup, detector calibration, and preliminary testing, based in part on the knowledge gained during last semester’s scientific research work. This is to establish a baseline for future THz imaging developments.

1. THEORY

The theoretical foundation for understanding the key concepts involved in this research is provided in this section, including THz radiation, field-effect transistor (FET) detectors, patch antennas and optically pumped terahertz lasers.

1.1. THz radiation

Terahertz radiation occupies the range between infrared and microwave radiation in the electromagnetic spectrum, exhibiting properties of both. It falls within the range of 0.3 to 10 terahertz (Fig. 1). Similar to infrared and microwave radiation, terahertz radiation propagates through a single medium in a linear trajectory and is non-ionising. Terahertz radiation, like microwave radiation, can penetrate many non-conducting materials. It can pass through clothing, paper, cardboard, wood, masonry, plastic, and ceramics. However, its penetration depth is typically shallower than that of microwave radiation.

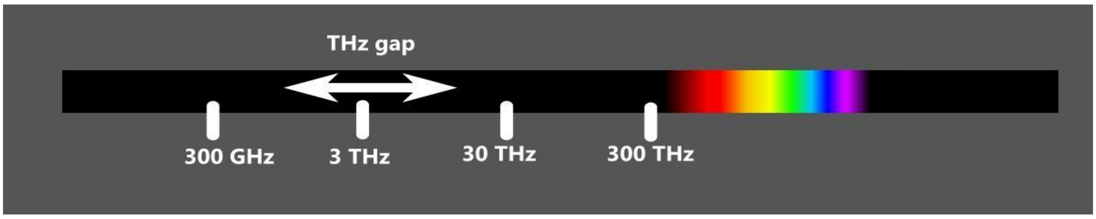

Fig. 1. Scale showing the THz gap.

The THz range falls into a region of the electromagnetic spectrum where the frequency is much higher than that of electronic counter devices. It is difficult to generate and modulate THz signals using conventional electronic devices such as transistors. In principle, transistors and other electronic devices based on electric transport are limited by a cut-off frequency of around 300 GHz [2]. One of the main physical reasons for this limit is the transit-time effect. The functioning of a transistor is dependent on the movement of electrons across its internal channel. With an increase in signal frequency, the time taken for an electron to traverse a given distance becomes significant. If the signal switches faster than the electrons can reach the other side, the transistor fails to amplify [4]. Bearing this in mind, conventional electronic devices have a limit of 50 GHz because those operating above this limit are extremely inefficient [2].

At the other end of the THz spectrum, semiconductor lasers can produce effective radiation at very high frequencies of infrared, down to far infrared). However, the frequency range of these lasers is limited to around 3 THz for terahertz quantum cascade laser [5].

In order to bridge the THz gap, a wide variety of THz detectors have been developed, each with their own specific characteristics and advantages. These include optoacoustic Golay cells, as well as cooled and uncooled bolometers and pyroelectric detectors [6], [7], [8]. Newer detection methods use Schottky-barrier diodes, modified field-effect transistors and photoconductive antennas [9], [10], [11]. A comparison of the most common THz detectors is presented in Table 1.

Table 1. An overview of different terahertz detectors.

Detector	Operational frequency (THz)	Noise equivalent power (W/Hz$^{1/2}$)	Modulation frequency (Hz)	Detection mechanism	References
Golay Cell	≤30	10^{-10}-10^{-9}	20	Thermal	[12], [13]
Piezoelectric	≤30	(1-3)* 10^{-9}	10^{2}	Piezoelectric effect	[14]
Pyroelectric	≤30	10^{-9}-10^{-6}	2*10^{2}	Pyroelectric effect	[12], [15]
Nb microbolometer	≤3	5*10^{-11}	10^{6}	Bolometric effect	[16]
Bi micro bolometer	≤3	1.6*10^{-10}	10^{6}	Bolometric effect	[17]
HgCdTe hot-electron bolometer	≈0.03-2	4*10^{-10}	10^{8}	Hot-electron phenomenon	[18], [19]
InSb hot-electron bolometer	≤2.5	10^{-12}	5*10^{5}	Hot-electron phenomenon	[20], [19]
Schottky diodes	≤1.5	10^{-12} (bellow 1THz, increases above)	4*10^{10}	Rectification	[14], [21]
Si FET	≤30	1*10^{-10}	5*10^{6}	Plasma wave	[22], [23], [24]
FET (AlGaAs/GaAs)	≤30	1*10^{-9} 1*10^{-7}	-	Plasma wave	[25], [26]

The terahertz gap is where traditional electronics and optics meet, and it is an area where we currently lack efficient tools and machines. This, in turn, motivates the creation of specialised detectors that span this region. Operating in this frequency range enables us to perform non-destructive security screenings, medical diagnostics and industrial quality control [27] without exposing people to the health risks associated with high-energy radiation [28]. By bridging this gap, we can enable high-speed communications and molecular spectroscopy that can be used in astronomy [29].

1.2. Field-Effect Transistor (FET) detector

In this work, for terahertz wave detection we use field-effect transistor-based detector. This technology offers ultra-fast response time, high responsivity, seamless integration with Complementary metal-oxide-semiconductor (CMOS) processes [30]. Additionally, other sensors or sensor structures may be implemented in parallel with the main process, enabling a highly scalable solution. These devices can be highly tuned by gate, doping and the channel structure itself [30], [31].

Terahertz radiation detection using FET is made possible by transistors' non-linear properties. These show up as rectification of alternating current induced by THz radiation. This results in direct current voltage between source and drain. This can be described as a photovoltaic effect because the dc voltage is proportional to radiation power. In order for this mechanism to take place, an asymmetry is required between source and drain to induce DC voltage. This can be achieved by making source and drain contact pads different or by introducing a parasitic external capacitance [3]. Additionally, asymmetry can be achieved by specifically designing an antenna that is connected to the one side of the transistor channel (Fig. 2).

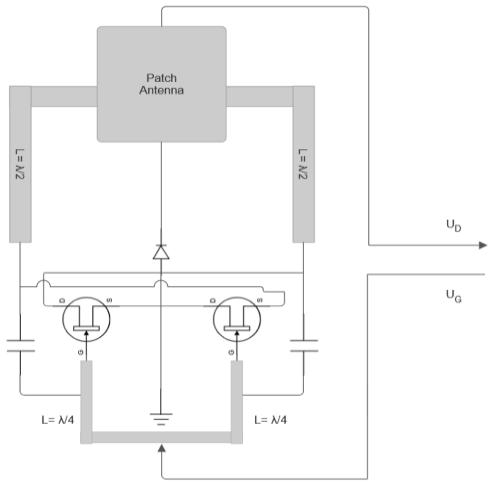

Fig. 2. Detector chip scheme showing both the patch antenna and the transistors.

Fig. 3 shows a field-effect transistor (FET), where incoming radiation creates an alternating current (AC) voltage with an amplitude of U_{AC} only between the source and gate. No direct current (DC) exists between the source and drain. The channel in this FET can be modelled using distributed gate-to-channel capacitance, distributed inductance, and channel resistance. The channel resistance depends on the gate and drain voltages, as well as the electron concentration in the channel. When the spatial variation scale of U(x) is larger than the gate-to-channel separation d (i.e., when using the gradual channel approximation), the electron concentration in the channel is given by the following equation [3]. The distributed inductance represents the kinetic inductance due to electron inertia and is proportional to the electron's effective mass (m). The Drude model accounts for electron inertia:

$$Z = R(1 + j\omega\tau) = R + j\omega L \qquad (1)$$

where Z is impedance, R is resistance, Ω is frequency, τ is momentum relaxation time and L is the kinetic inductance.

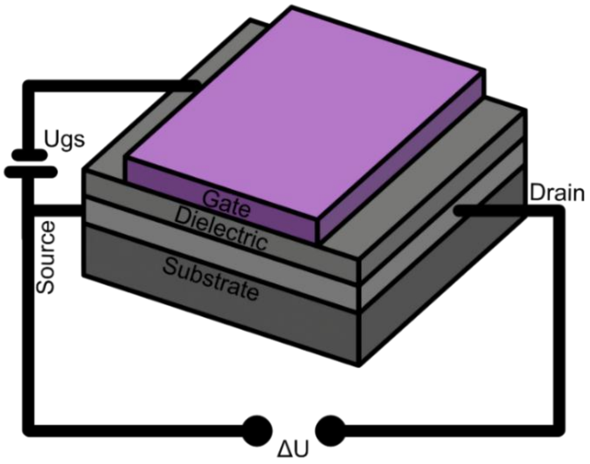

Fig. 3. Principle scheme of FET.

Under static conditions and when the drain current is 0 A, Voltage is equal to static voltage swing. Two modes of operation can be distinguished depending on frequency omega – high and low [3]. These in turn can be further divided into long and short gates. These regimes are illustrated in Fig. 4.

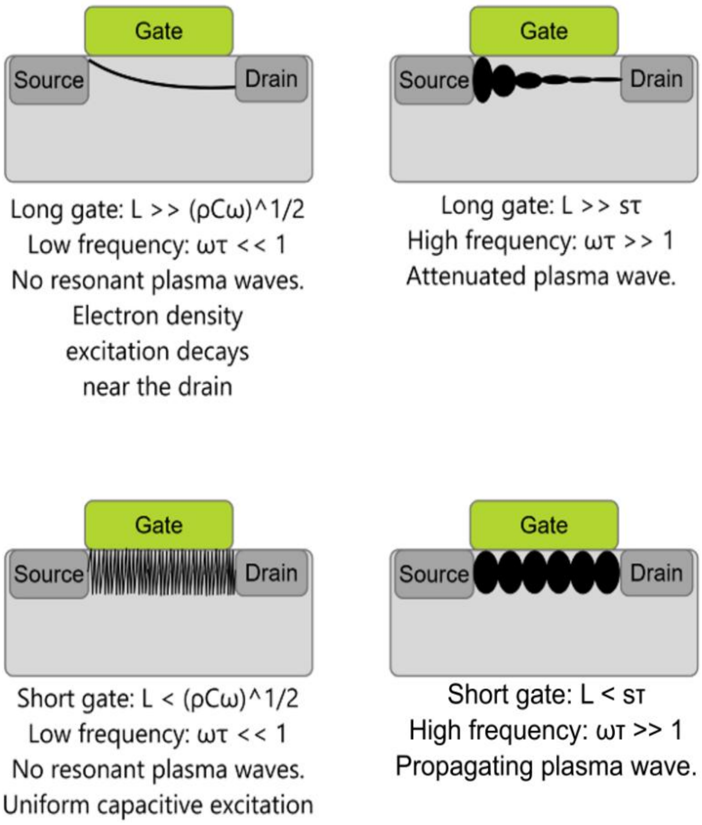

Fig. 4. Schematic representation of carrier density waves in different regimes.

1.3. Patch Antennas

Microstrip patch antennas are widely used in the field of communication, where they are employed for a variety of applications. Depending on the materials used the antennas can cover a broad frequency range. For instance, graphene based microstrip line fed patch antenna on silicon dioxide substrate can achieve frequencies of 12.2-13.8 THz [32]. Other examples show that stacked microstrip antenna has a range of up to 8.2 THz [33]. At lower frequencies, the physical properties of the antenna (size and weight) are often the limiting factor, while at higher frequencies, mechanical tolerances and electrical losses often dominate antenna designs [34].

Figure 5 shows the structure of the patch antenna. It consists of a very thin metallic strip (patch), which is placed a small fraction of a wavelength (h) above a ground plane. Typically, h is between $0.003*\lambda_o$ and $0.05*\lambda_o$, where λ_o is the free-space wavelength.

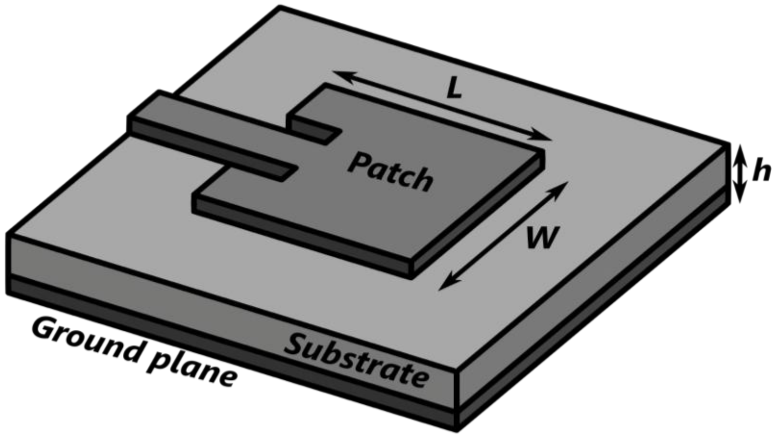

Fig. 5. Microstrip patch antenna structure.

The maximum radiation pattern of the patch, also known as the broadside radiator, depends on the patch itself. For a rectangular patch, L represents the length of the patch, which is usually between $\lambda_o/3$ and $\lambda_o/2$. This value is proportional to the antenna's frequency. W represents the width of the patch, which must be smaller than λ_o, but not too small, otherwise the antenna will become a microstrip line and will no longer radiate [35]. The width controls the input resistance of the patch antenna. The ground plane is separated from the patch by a dielectric sheet (the substrate).

The radiation pattern of a patch antenna is characterised as broadside, with maximum field intensity perpendicular to the patch's surface [36]. In practice, the main lobe is accompanied by minor side lobes and a back lobe in the antenna's fundamental modes (TM10 or TM01). Although higher-order modes such as TM30 can be excited, they often result in limited directivity (D) due to the presence of high secondary lobes that distort the radiation distribution. Single-element microstrip patch antennas typically exhibit low directivity of approximately 6–7 dBi [37]. This can be reduced further by optimising the patch antenna's structure. One option is to use patch arrays, which increase gain but introduce feeding network losses. Other methods supported by the literature for focusing radiation include the use of stacked patches [38], superstrates [39], zero-index metamaterials [40].

The effective area (A_{eff}) describes an antenna's ability to extract power from an incident electromagnetic plane wave [41]. It is mathematically linked to the operating wavelength and antenna's directivity via the following equation:

$$A_{eff} = \frac{\lambda^2}{4\pi} D \qquad (2)$$

where λ is the wavelength and D is the directivity.

1.4. Optically pumped terahertz laser

A Terahertz laser makes use of the rotational levels of polar molecules between population inversions to generate terahertz waves. THz lasers are roughly divided into two types of pump lasers: pulsed and continuous. The energy of a pulsed THz laser can reach several joules, while the power of a continuous THz laser can reach several hundred milliwatts [42].

A simplified three level system is depicted in figure 6. The transfer of molecules occurs from the rotational level 1 in the ground vibrational level to the rotational level 2 in the excited vibrational level. The THz laser emission occurs between pumped rotational level and an adjacent, lower-lying level. The rate equation model for this system is as follows:

$$\frac{dN_1}{dt} = N_{21}W_p + \left(f_1 N_{V_0} - N_1\right)W_C \quad (3)$$

$$\frac{dN_2}{dt} = -N_{21}W_p - N_{23}W_T + \left(f_2 N_{V_1} - N_2\right)W_C \quad (4)$$

$$\frac{dN_3}{dt} = N_{23}W_T + \left(f_3 N_{V_1} - N_3\right)W_C \quad (5)$$

$$\frac{dN_{V_0}}{dt} = N_{21}W_p + N_{V_1}W_{V_1} \quad (6)$$

$$\frac{dN_{V_1}}{dt} = -N_{21}W_p - N_{V_1}W_{V_1} \quad (7)$$

where N_i (i = 1, 2, 3) are the populations in cm^3 at the lower and upper laser levels, N_{21} is the difference in occupation between levels 2 and 1 (this value is always negative), and N_{23} is the difference in occupation between levels 2 and 3 (this value is always positive). G_i is the degeneracy of level i, N_{V_o} is the total number of molecules in cm^3 in all rotational levels of the ground vibrational level, f_i is the Boltzmann factor, W_c is the collision rate among the rotational levels of a vibrational level to establish equilibrium, W_{V1} is the vibrational relaxation rate, and W_p and W_T are the induced transition rates of optical pumping and simulated THz emission, respectively. The latter is expressed by the following equation:

$$W_{p(T)} = \frac{\lambda^2 I_{p(T)} S(\nu)}{8\pi h\nu t_{sp}} \quad (8)$$

where $I_{p(T)}$ is the beam intensity, λ is the wavelength, and ν is the frequency; TSP is the spontaneous lifetime; and S(ν) is the line width function.

Terahertz radiation occurs when the rate of induced transitions is much larger than the rate of collisions. The following comparison must be true for it to occur: $W_t \gg W_c$ and $Q_{Emax} = 1/2 * \lambda_p/\lambda_\tau$.

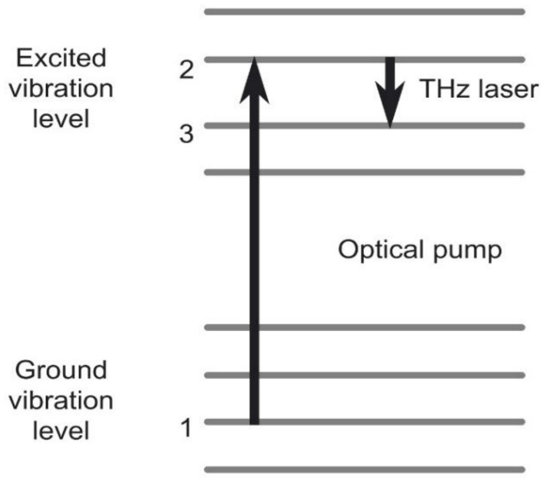

Fig. 6. Level diagram for optically pumped THz laser.

High-repetition frequency pulse-optically pumped terahertz lasers can be applied in high-speed terahertz imaging, terahertz laser radar, medical diagnosis and other fields [43].

1.5. Directivity

The directivity of an antenna is defined as the ratio of the radiation intensity in a given direction to the radiation intensity averaged over all directions. The total power radiated by the antenna is divided by 4π to find the average radiation intensity [44]. If no direction is specified, the direction of maximum radiation intensity is implied. It can be written as follows:

$$D = \frac{U}{U_0} = \frac{4\pi U}{P_{rad}} \tag{9}$$

where U is radiation intensity, U_0 is radiation intensity of an isotropic source and P_{rad} is the total power.

The directivity of an array is a measure of how effectively it directs energy in a particular direction. The directivity is defined by the array geometric function. This is if the antenna elements are isotropic. For a linear array operating in transmit mode, the geometric array function is defined as the radiated power density in the direction of the main beam maximum, divided by the average power density from the array [45]. For a symmetrical array with spacing between the antenna elements of λ/2, the array directivity, D, is given by the following expression:

$$D = \frac{\left[\sum_{-n_z}^{n_z} U_n\right]^2}{\sum_{-n_z}^{n_z} U_n^2} \quad (10)$$

where n_z is antenna elements positioned in z-axis.

2. TECHNOLOGICAL METHODOLOGY OF TERAFET FABRICATION

This work involved developing a THz detector from the initial design stage onwards. To establish a baseline for these designs, numerical simulations of the TeraFET antennas were conducted alongside an evaluation of their current-voltage characteristics. The next step was researching operational amplifiers (op-amp) that would suit the detector's needs. After selecting a suitable op-amp, the entire electrical circuit was modelled to validate its behaviour. Using the information gathered from the operational amplifier characteristics and the modelling results, the detector was assembled. This entailed soldering components such as operational amplifiers, resistors and capacitors to a ready-made PCB, gluing a mirror and antenna on top and finally assembling the components into a stand. Next, we prepared a measurement setup consisting of a mirror system that guided the THz wave onto the specimen. Measurements were taken by scanning the antenna area to determine the angular dependency of power.

2.1. Fabrication and simulation of TeraFET antennas

The antenna components of each detector were fabricated using the 65-nm foundry process of the Taiwan Semiconductor Manufacturing Company. While the antennas in this study were designed primarily for a frequency of 2.52 THz, Figure 7 shows a picture of the first detector featuring patch-antenna-coupled TeraFETs with different patch sizes. These variations enable resonance frequencies to vary from 0.5 THz to 2.5 THz. The specific antenna used in this study is indicated in the figure. Figure 8 illustrates multi-pixel antenna array chips in both 3x3 (a) and 4x4 (b) configurations. Each unit has a uniform structure consisting of a 20 x 20 µm copper patch antenna with mounted on a 75 x 75 µm dielectric silica substrate. All the antenna microchips used in this study were designed by Prof. Alvydas Lisauskas.

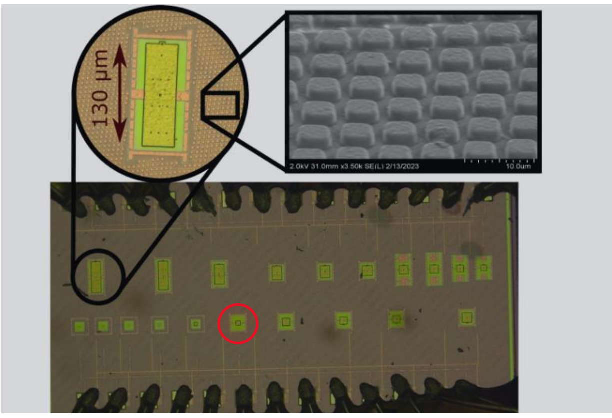

Fig. 7. Antenna microchip with two rows of patch-antenna-coupled TeraFETs, with ten devices in each row [46]. The specific antenna used in this study is marked red.

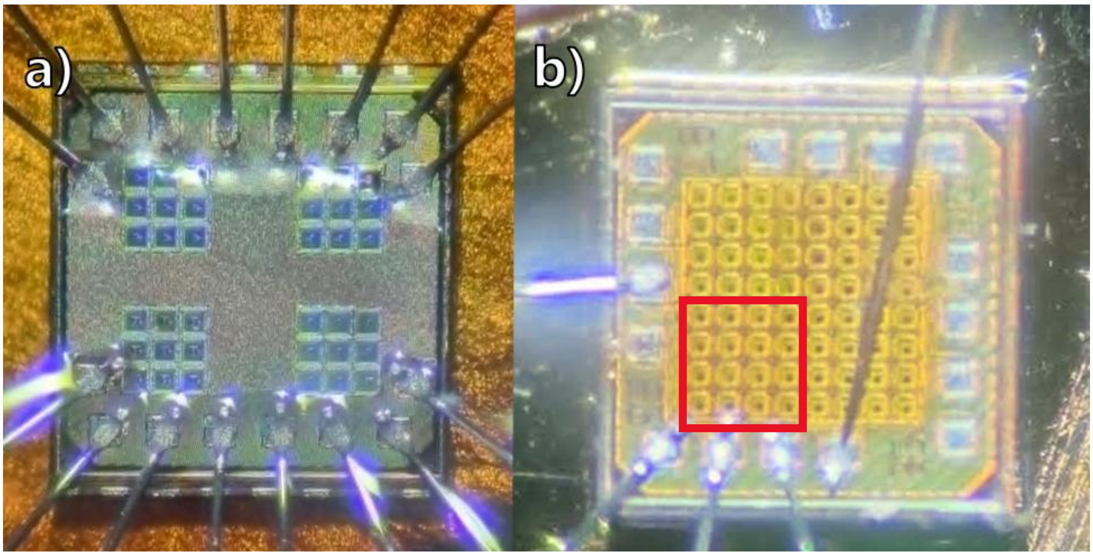

Fig. 8. Multi-pixel antenna arrays of a) 3x3 and b) 4x4 configurations (used area is marked in red).

To validate the previously mentioned resonant frequency, a modelling result was required, so a simulation of a single-patch antenna was performed using Keysight's Advanced Design System (ADS), as shown in Figure 9. To emulate the antenna, a substrate stack was chosen with the exact measurements and dielectric constants of the original design.

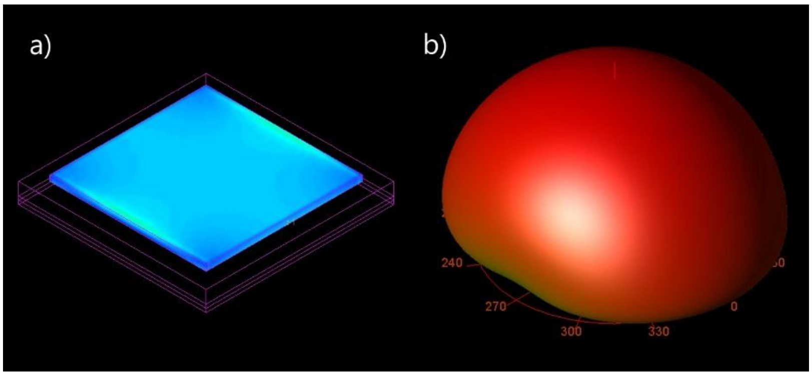

Fig. 9. Simulation setup using ADS, here a) is patch antenna with visible feed points (lighter blue) and b) radiational pattern of said antenna.

A 20 x 20 µm patch in the conductive layer (Fig. 9a) was chosen to act as the radiating element of the patch antenna. To excite the radiating element, a symmetrical feed geometry was implemented. The resulting 3D radiation pattern (Fig. 9b) shows a clearly defined broadside lobe, which confirms that the energy is directed perpendicular to the substrate plane, as is typical of a patch antenna.

The parameters of resonant frequency, directivity, gain and effective area were derived from the simulation results for a single patch antenna.

2.2. Analysis of the current-voltage (IV) characteristics of TeraFET transistors

The IV characteristics of the TeraFET antennas were characterised using an Agilent B1500A Semiconductor Device Analyser to evaluate the DC performance and biasing requirements of the detector. The measurement used a multi-channel synchronous sweep setup to accurately map the device's response. The gate was controlled by a linear primary voltage ramp ranging from 0 V to 1 V in 101 discrete steps, while the drain underwent a secondary sweep ranging from -5 mV to 5 mV in 10 mV increments. A constant protection bias of 1.6 V was maintained throughout to enable the device.

The physical integrity of the 65-nm structures was ensured by integrating limits into the measurement routine. The gate sweep was limited to 250 µA, while the drain and protection channels were assigned thresholds of 1 mA and 10 mA, respectively.

2.3. Research for the most suitable components for amplifying stage

To get the best results from the assembled detectors, an optimal operational amplifier is needed. In an electrical circuit, an operational amplifier acts as a signal amplifier. Since THz detectors are considered very sensitive equipment that operates at very high frequencies, optimal parameters are needed for the devices. These include gain bandwidth, noise (both thermal and 1/f), and corner frequency. These parameters are the main criteria for searching for a suitable operational amplifier. Table 2 lists various components that were under consideration. Among these, the OPA858 is clearly the most suitable operational amplifier for the detector, with the best gain bandwidth of 5.5 GHz, a high 1/f noise bandwidth of 200 kHz, and a relatively small thermal noise of 2.5 nV/√Hz.

Table 2. List of operational amplifiers.

part number	noise, nV/√Hz	gain bandwidth, MHz	1/f noise bandwidth, Hz
op1177armz	8	1.3	-
op27gpz	3.5	8	2.7
ad817arz	15	50	-
LT1792	4.2	5.6	30
LT1793	4.2	5.6	30
OPA2354	6.5	100	300k
OPA211AIDR	1.1	80	20
OPA858	2.5	5500	200k
LT6200	0.95	165	600
OPA843	2	800	60k
OPA818	2.2	2700	15k
OPA859	3.3	900	200k
ADA4625-1	3.3	18	-
OPA827	4	22	40
LMH6624	0.92	1500	7k
OPA814	5.3	250	2000
OPA847	0.85	3900	20k
OPA856	0.9	1100	30k
OPA828	4	45	50

2.4. Simulation of the electrical circuit

Electrical circuit simulations were carried out to determine whether the chosen operational amplifier was suitable for the scheme and would function as required. This was done using LTspice software.

Electrical circuit simulations were carried out to determine whether the chosen operational amplifier was suitable for the scheme and would function as required. This was done using LTspice software. The first simulation was performed to analyse the open-loop gain of the individual operational amplifiers. This was done to confirm that the op-amps act according to both the manufacturer's datasheet and our requirements. To measure the open-loop gain of the OPA211 and OPA858, a simple open-loop circuit was modelled (see Figure 10 and Figure 11, respectively). In both cases, a large inductance was introduced to establish a direct path for DC feedback but act as an open circuit for the AC signal. The large capacitance enabled the AC signal to travel to the operational amplifier's input without shorting out the DC bias. A small signal AC generator was used for the voltage source. The simulation parameters are shown in Figure 10 and Figure 11. The gain and phase dependence on frequency were measured.

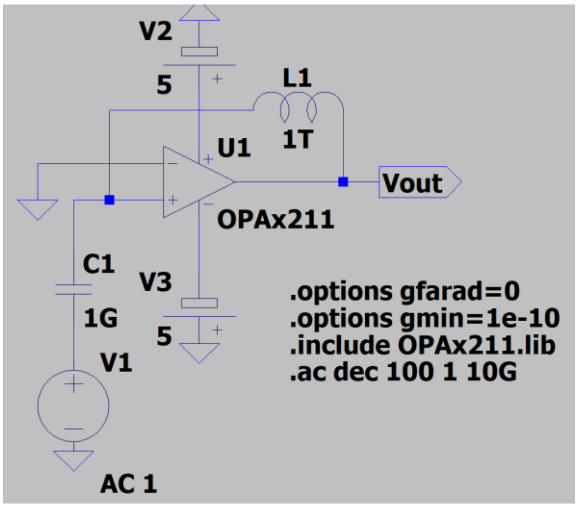

Fig. 10. Open loop gain circuit for OPA211.

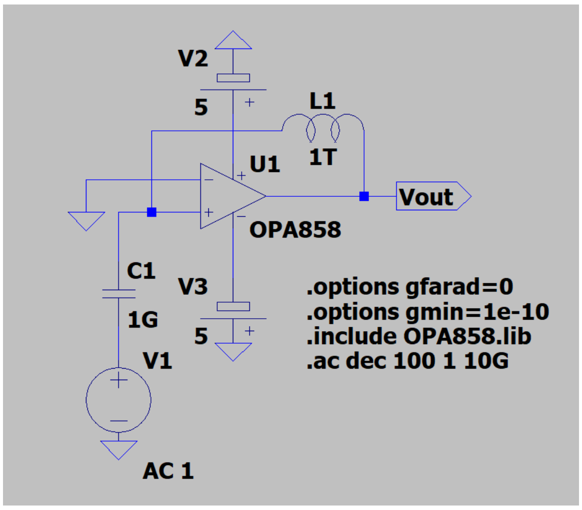

Fig. 11. Open loop gain circuit for OPA858.

Figure 12 shows the results of open loop gain measurements performed on the OPA211 operational amplifier. As can be seen from the graph, the open-loop gain starts at approximately 130 dB. These results align almost exactly with the typical values introduced in the datasheet. The dominant pole begins to roll off at around 10 Hz, with the gain dropping at a consistent rate of -20 dB per decade. At around 45 MHz, the gain reaches the unity-gain crossover point. These values closely resemble those provided in the datasheet.

At the unity-gain crossover point, the phase is approximately -120°. By calculating the difference from -180°, a margin of 60° is obtained. This indicates that the amplifier is highly stable and closely resembles the data sheet value of 62°.

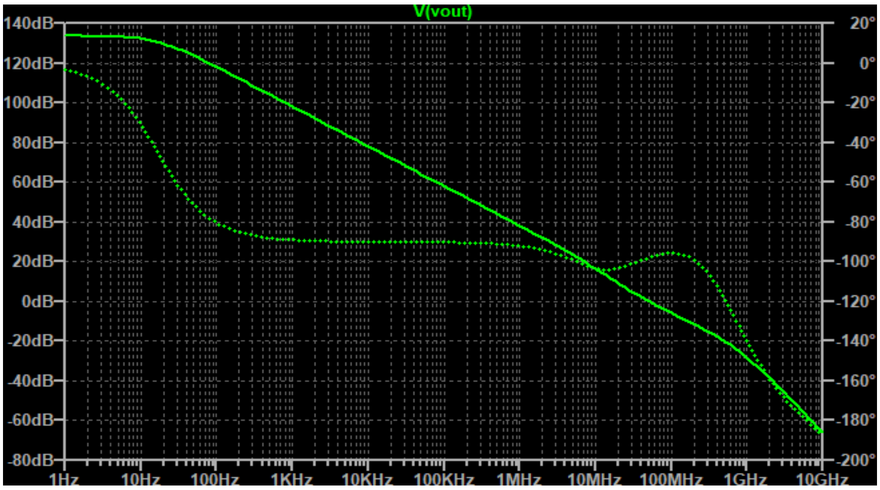

Fig. 12. Results of open loop gain simulation performed on the OPA211.

Figure 13 shows the open-loop gain measurement results for the OPA858 operational amplifier. As with the OPA211 measurements, the open-loop gain starts at a value similar to that presented in the datasheet, but this time at 80 dB. A comparison of the two shows that the OPA858 has a lower gain value than the OPA211, but a significantly higher bandwidth. This indicates superior performance at higher frequencies.

In the case of the OPA858, the unity-gain bandwidth crosses the 0 dB line at around 5.5 GHz. This result is exactly as depicted in the datasheet. Comparing the two frequencies shows that this amplifier can handle higher frequencies: 5.5 GHz compared to 45 MHz.

The phase response (dotted line in Figure 13) remains at 0° up to around 100 kHz. This enables the operational amplifier to be used in high-frequency applications. At the gain-unity point, the phase is -140°, leaving only 40° of phase margin. This indicates that the amplifier is not stable near the unity gain, and that it is designed for use in circuits with much larger gains.

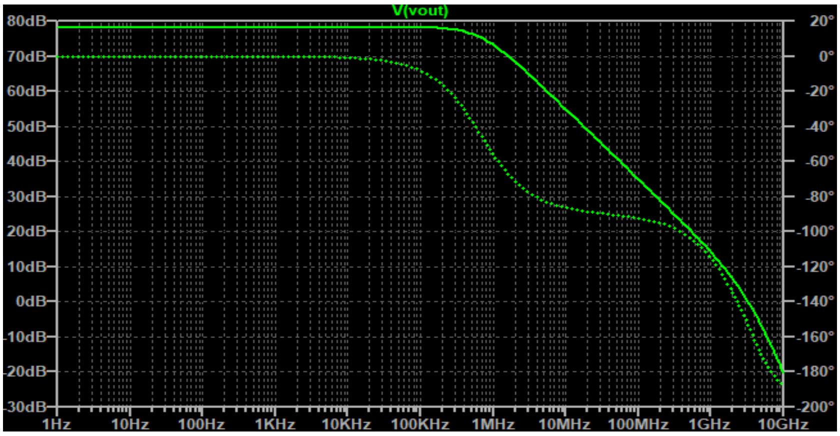

Fig. 13. Results of open loop gain simulation performed on the OPA858.

After confirming that each operational amplifier worked as intended, the two op-amps were connected in series to form a multistage amplifier. The circuit is shown in Figure 14. As in the previous simulations, a small signal AC generator was used. However, this time the circuit was designed as a closed loop, with resistors representing a real-world circuit. The values of the components and simulation parameters are provided in Fig. 14. The gain and phase dependence on frequency were measured.

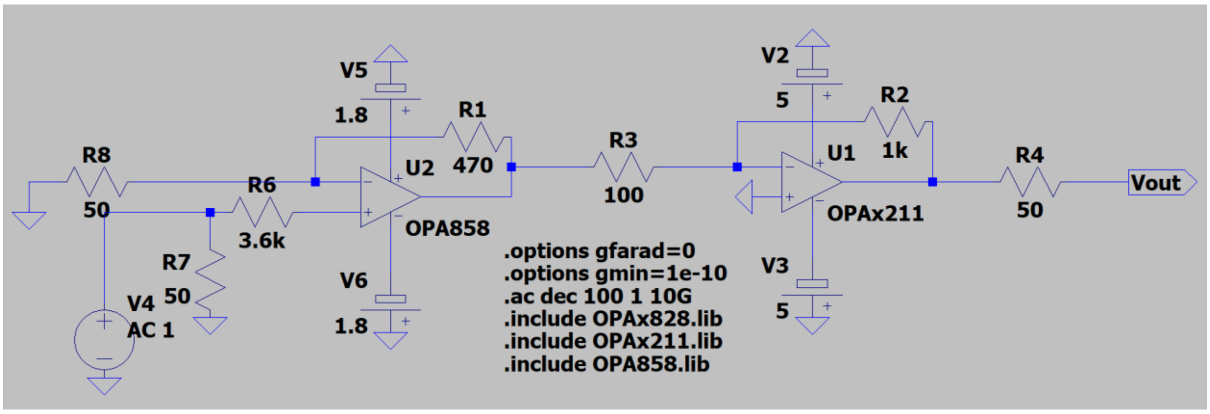

Fig. 14. Circuit of a multistage amplifier

The simulation result of the multistage amplifier is presented in Figure 15. The graph shows a combined closed-loop gain of 40 dB. This indicates that the circuit's total amplification is 100 times. The gain remains relatively constant up to around 200 MHz, which is an excellent result for a high-gain multistage amplification system. Despite the OPA858 having a gain bandwidth of 5.5 GHz, the operational amplifier OPA211 reduces the system's gain bandwidth product to 200 MHz.

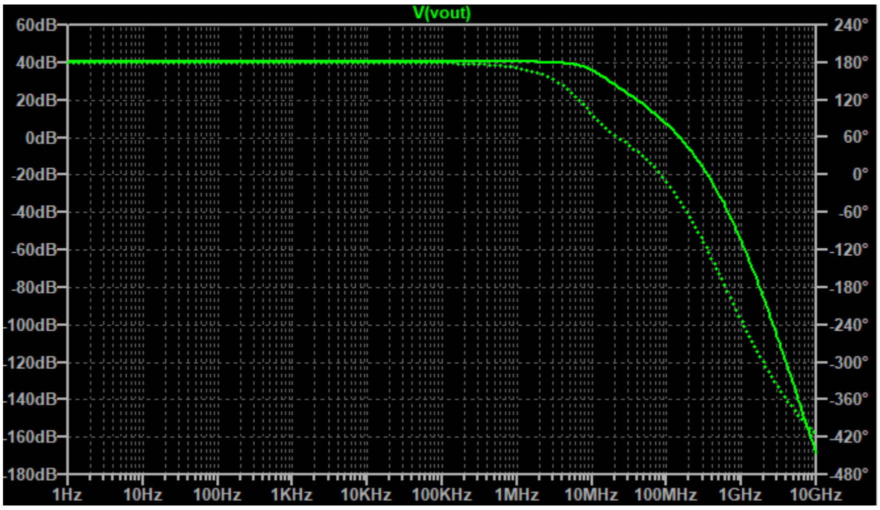

Fig. 15. Results of the multistage amplifier simulation

The total phase shift accumulated through both stages is indicated by the phase plot (shown by the dotted line in figure Fig. 15). As the frequency increases, the phase drops much more steeply. This is because the system is now dealing with the combined internal poles. The phase crosses 0 dB at 60°, which is an excellent result for the phase margin of 120°. This indicates that the multi-stage amplifier is highly stable around the unity-gain crossover point.

2.5. Preparation of PCB boards

After confirming that the operational amplifier would work well with the rest of the circuit, the PCBs were assembled.

First, a 500 μm gold-plated silica wafer was glued in the middle of the first stage of amplification to act as a backdrop (Fig. 16). This was done by mixing 1:10 parts (0.004 g and 0.041 g) of high-temperature, vacuum-compatible, low-outgassing epoxy 353NDPK. Then, the PCB with the epoxied mirror was heated for 30 minutes at 100°C to allow the epoxy to harden.

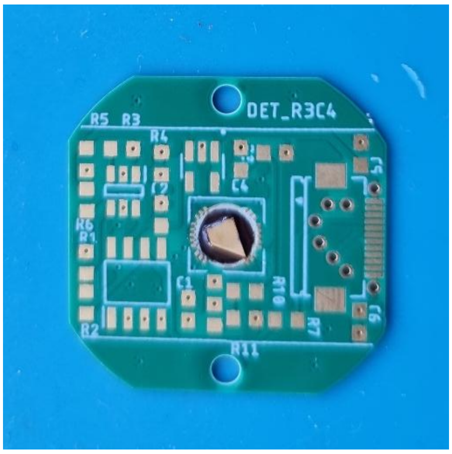

Fig. 16. PCB with gold-plated silica wafer glued in the middle.

With the mirror in place, the components of the electronic circuit were soldered into their respective positions. They were soldered according to their sensitivity to heat from the soldering iron, with the most sensitive components left for last. First, the resistors and capacitors were soldered, followed by the connectors, transistors and operational amplifiers (Fig. 16a). Following all the soldering, the detector chip (that includes both the transistor and the antenna) was glued onto the mirror backdrop. This was done with the same epoxy described previously. A high-precision microscope equipped with a linear scale was used to determine the exact centre of the PCB to secure the antenna in the appropriate place (Fig. 17b).

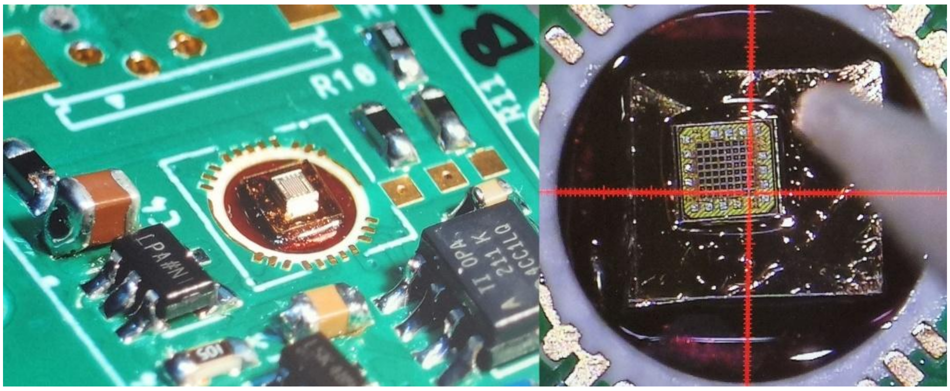

Fig. 17. a) PCB with all the components soldered and the detector chip, glued in place; b) process of glueing the detector chip to the board.

The bonding process was performed to allow the current to flow from the antenna to the rest of the electronic circuit. This process was carried out using the F&S Bondtec 5630i thin wire wedge-to-wedge bonder (Fig. 18).

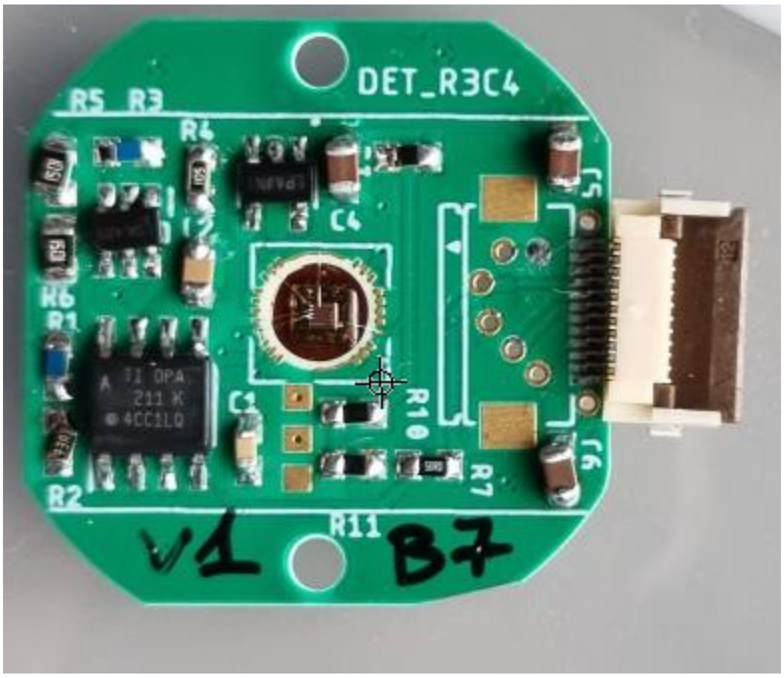

Fig. 18. First step amplifier fully assembled and detector chip contacts bonded to the PCB.

2.6. Assembly of the detector

Once both PCBs were prepared, the entire detector needed to be assembled. First, the two amplification stages were connected by a twelve-pin ribbon cable. Then, to safely work with and handle the detector, the PCBs were mounted onto a standard 30 mm CP33 cage plate by Thorlabs (Fig. 19). This cage plate was chosen because it is compatible with the mirror measuring system described in the next chapter.

After assembly, an initial test was conducted to determine if the detector was functioning properly. This was done by connecting an external direct current source to the operational amplifier's power supply. The source provided around 5 V to both the positive and negative terminals, which was the desired outcome.

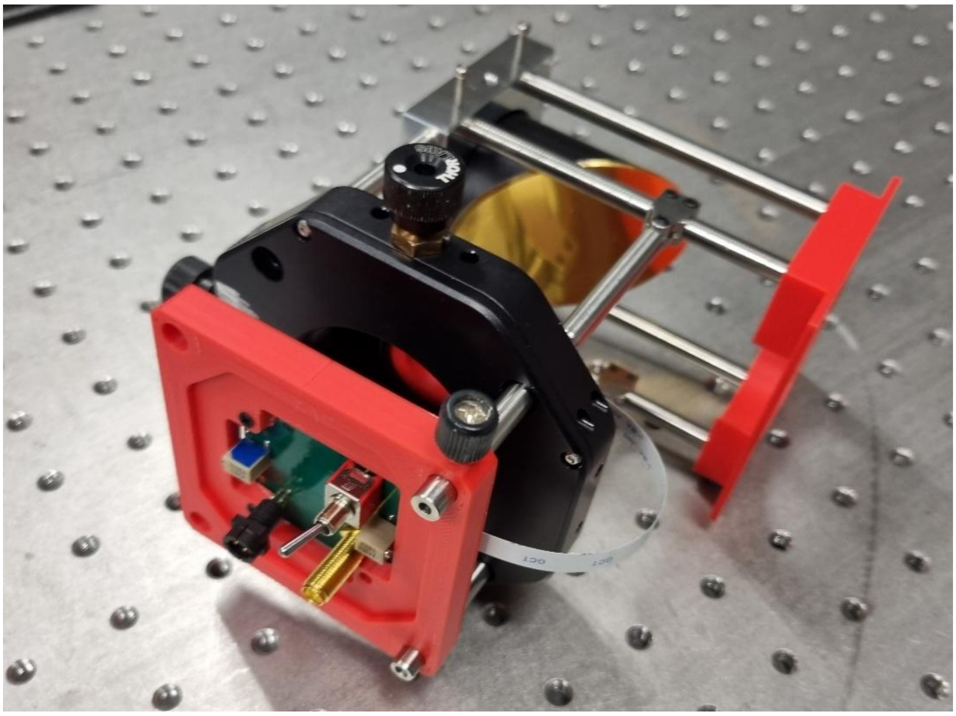

Fig. 19. Detector fully assembled.

2.7. Measurement setup

An optical chopper is commonly employed to modulate the intensity of laser pulses during the generation of terahertz waves. This technique is used to measure signals with noise levels greater than the useful signal. Lock-in measurements require a reference frequency to calibrate the system and ensure accurate results [47]. Typically, this frequency remains constant throughout the experiment, supplied by an oscillator or function generator. The lock-in amplifier then detects the response from the detector at this frequency. Noise signals at frequencies other than the reference frequency are not included in the measurement and do not affect it. Both techniques are used to accurately measure the THz detector characteristics in this study.

Figure 20 shows the main schematic block diagram of the THz measurement setup. This can be categorised into sections. First is the THz wave generator, followed by the mirror system, the chopper and aperture, the pyroelectric detector and lock-in system, and finally the detector itself.

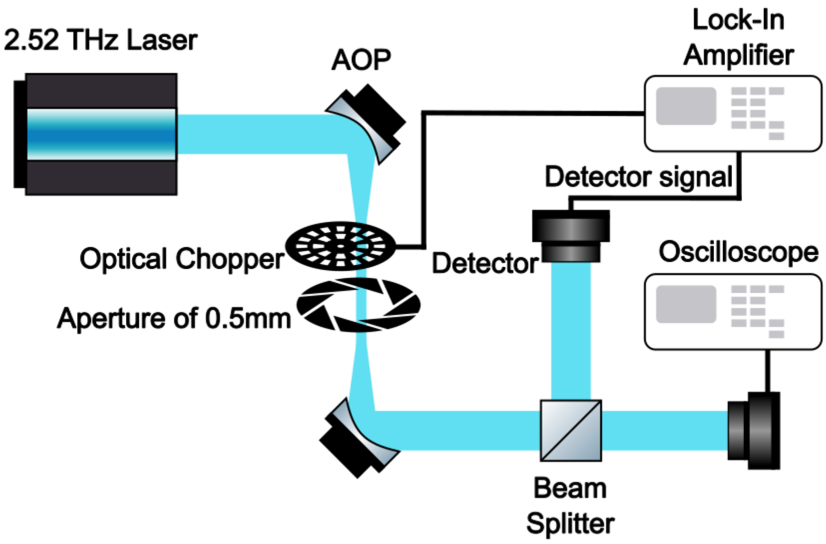

Fig. 20. Main schematic diagram of the THz measurement setup.

For the Terahertz wave generation, the Edinburgh FIRL-100 FIR (THz) Laser was used. The FIRL-100 is a device that incorporates both a CO_2 pump laser and a FIR laser, with these two components being housed within a single integrated structure. The CO_2 section provides 80 lines ranging from 9.1 µm to 10.9 µm and features a single discharge tube with a flowing gas, providing more than 50 W for the strongest lines. Internal profiling of the tube and the use of high-quality optics ensure mode performance (M2 <1.25). The resonator design is based on the reliable PL5 laser, featuring a diffraction grating, two ZnSe Brewster windows, and a piezo-ceramic-mounted ZnSe output coupler. The carbon dioxide laser output is coupled into the FIR laser via a pair of control mirrors and a zinc selenide focusing lens.

This study used a CO_2 laser with a gas mixture consisting of CO_2, N_2 and He. The laser had a power output of 9 W and a pressure of 27 mbar in the CO_2 resonator. The THz resonator, which used CH_3OH gas, had a pressure of 0.2 mbar and generated 2.52 THz frequency and 118.8 µm length waves. Additionally, a 0.5 mm aperture is used to filter out spatial distortions and unwanted reflections, thereby establishing a clean, uniform THz beam. This ensures the radiation hitting the detector has a strictly defined diameter. It also ensures a predictable Gaussian profile.

The SNR and sensitivity of terahertz detectors at room temperature is inferior to that of cryogenically cooled ones [48]. The problem primarily derives from unwanted noise caused by background radiation, including black body radiation. Additionally, 1/f noise is significantly higher due to room temperature operation. These noises are problematic because they are directly proportional to temperature and inversely proportional to sampling duration. The first steps in reducing noise were taken in the schematic design phase. By designing an amplifying PCB ourselves, we were able to ensure that the DC signal was as clean as possible. This means that the circuit used in this work has a 1/f value as low as possible. Additionally, to bypass this problem, the Model 7265 DSP Lock-in Amplifier was used. This instrument closely resembles a homodyne direct conversion receiver and effectively acts as a high-Q bandpass filter, distinguishing between the desired measurable signal and the background noise.

In this work, the lock-in amplifier takes two readings: the frequency of the optical chopper and the signal of the TeraFET detector at this modulation frequency.

2.7.1 Measurements

The measurements were conducted in two stages. First, the output from the Edinburgh FIRL-100 (FIR) laser was mapped using a detector mounted on an automated X-Y translation stage. The beam's centre was identified, and the coordinates of peak intensity were determined by performing a raster scan. This step ensured that the detector was positioned at the optimal point for the next stage. This step involved positioning the detector directly in the path of the upcoming THz wave, ensuring the polarisation remained horizontal.

Once the optimal point had been established, angular measurements were taken to characterise the radiation pattern. The detector was rotated around the optical axis, and the power dependency was recorded across the angular range from −180° to 180°.

3. RESULTS OF TERAFET DETECTORS CHARACTERISATION

The following results summarise the experimental and numerical data that were used to evaluate the performance of the THz detectors. The analysis includes an examination of the current-voltage characteristics, spatial signal maps and angular radiation profiles of single-pixel and multi-pixel (4x4 and 3x3) array detectors.

3.1. Results of the IV characteristics analysis of TeraFET antennas

Figure 21 illustrates the transfer characteristics (resistance versus gate voltage) for two different teraFET multi-pixel antenna configurations: a 4 × 4 array (part a) and a 3 × 3 array (part b). These curves are essential for identifying the optimal operating point for THz detection, since the device's responsivity is directly related to the nonlinearity of its resistance.

Both graphs depict typical FET behaviour, in which the channel resistance is modulated by the gate voltage. At lower gate voltages (around 0.2 V for a and 0.1 V for b), the resistance is at its maximum value (10^7 Ω for a and around 10^9 Ω for b). This represents the high-impedance state, in which the carriers are depleted.

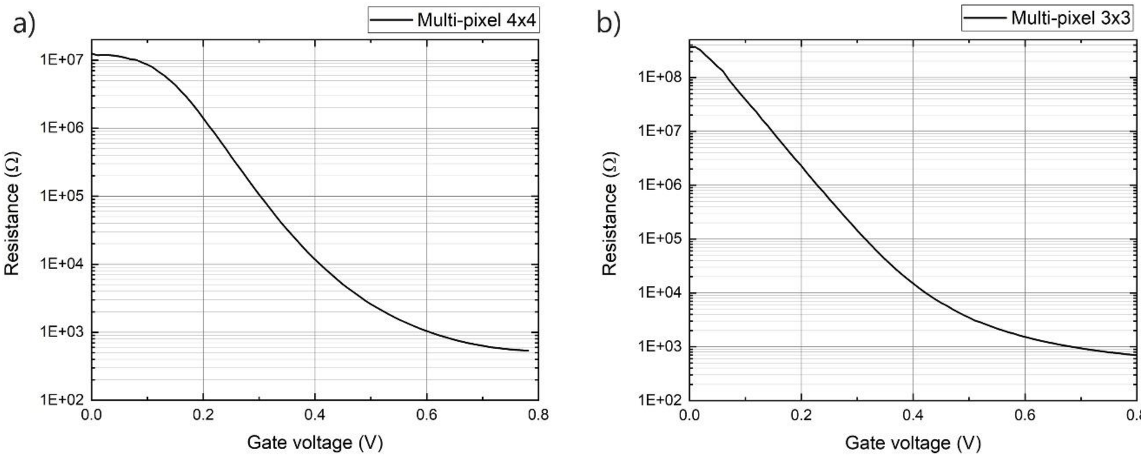

Fig. 21. Channel resistance dependence on the gate voltage characteristics of 4×4 (a) and 3×3 (b) multi-pixel TeraFET antennas.

As the gate voltage rises further, the resistance initially drops linearly, then exponentially, finally saturating at minimum values. For the 4x4 array, the minimum resistance is 500 Ω, and for the 3x3 array, it is 900 Ω.

The optimal working point for both antennas is a gate voltage of 0.6 V, which correlates to a resistance of 1000 Ω for 4x4 array and 2000 Ω for 3x3 array.

3.2. Results of TeraFET antenna simulations

The provided impedance plot (Fig. 22) confirms that the antenna is resonating successfully at the intended terahertz range. The primary peak, which occurs at approximately 2.4 terahertz, clearly demonstrates the patch's radiating performance. Although the resonance is well-defined, the exact peak has shifted slightly compared to the initial target. This can be attributed to discrepancies in the simulation parameters, such as the dielectric constants or thicknesses of the materials used in the substrate stack. Despite these minor variations, the behaviour of the real and imaginary impedance components demonstrates that the 20 x 20 µm patch operates as a resonator at the expected frequency.

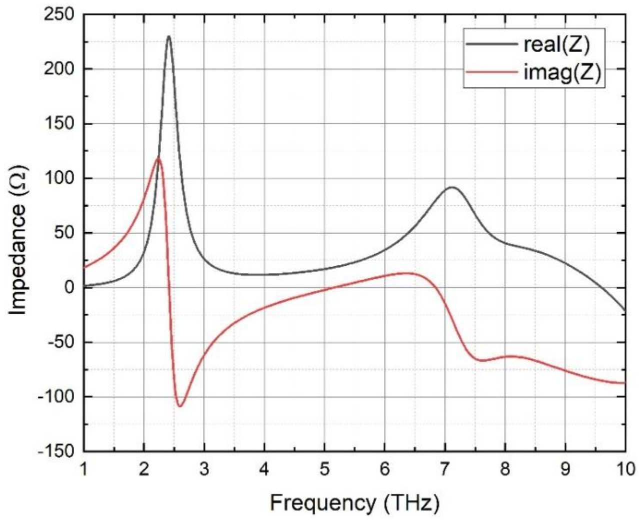

Fig. 22. Simulated impedance dependence of the TeraFET antenna on frequency.

The polar plot in figure 23 illustrates the antenna's directional characteristics, showing a peak directivity of around 6 dBi and a maximum gain of 0 dBi at the broadside angle of 0°. The broad, rounded shape of both curves confirms a wide beamwidth, meaning the antenna receives energy effectively over a large angular area rather than focusing it intensely in one direction. Additionally, the maximum effective area was calculated to be approximately 9×10^{-10} m².

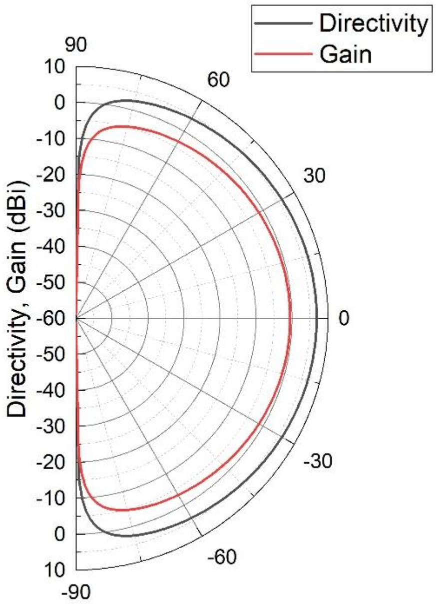

Fig. 23. Simulated angular dependence of the directivity and gain of a patch antenna.

3.3. Angular dependence measurement results without an aperture

The first measurement conducted on TeraFET detectors was the THz radiation sensitivity angular dependence. The graph (Fig. 24) shows a directional and asymmetric response, as opposed to the continuous one-lobe response that was expected. At the 0 mark, the intensity of the THz radiation is very small - around 25 μV.

The radiational pattern is separated in two distinctive lobes, that are of varying sizes, hence the asymmetry. Both lobes intensifies when the angle rises (or decreases for the negative angles) to a maximum or a peak intensity value and then slowly weakens to almost zero at 90° mark. The primary lobe is situated in the positive angular measurements and peaks around 370 μm. This maximum occurs at the degree of 55°. The secondary lobe peaks at around 161 μm at -45°.

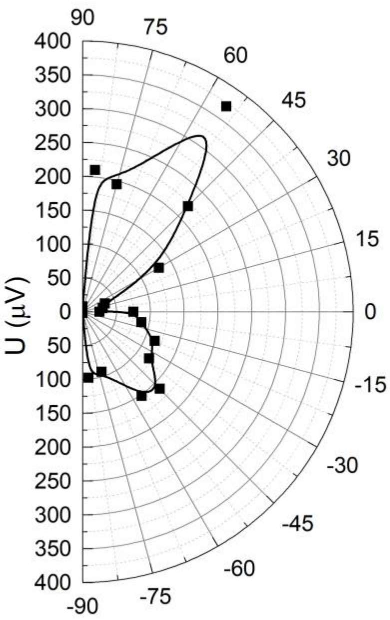

Fig. 24. THz radiation sensitivity angular dependence.

3.3.1 Mapping of the signal

Following the angular dependence measurements, the detector's signal was mapped to determine why the result differed from the expected one. Figure 25 part shows the signal intensity map, which was generated by raster-scanning the detector across the beam path to visualize its spatial energy distribution. The maximum value for this measurement was 0.74 mV. As opposed to a Gaussian profile the doughnut-shaped plot was observed in the measurements. This can be characterized by a central minimum and an asymmetric ring of high intensity are likely due to the spatial mode profile of the terahertz radiation emitted by certain sources. This shape may be a result of the THz emitter's specific design or of the emitted radiation's interaction with the optical components in the experimental setup [49]. Moreover, shapes like these are frequently linked to higher-order transverse electromagnetic modes in laser beams, where the intensity is spread out in a ring-like pattern around a central null.

The doughnut-shaped beam profile (Fig. 25) strongly correlates with the sensitivity peaks being pushed to the far sides, as seen in previous measurements (Fig. 24). The detector is likely picking up the high-intensity outer ring of the THz beam rather than a central core as the angle rises.

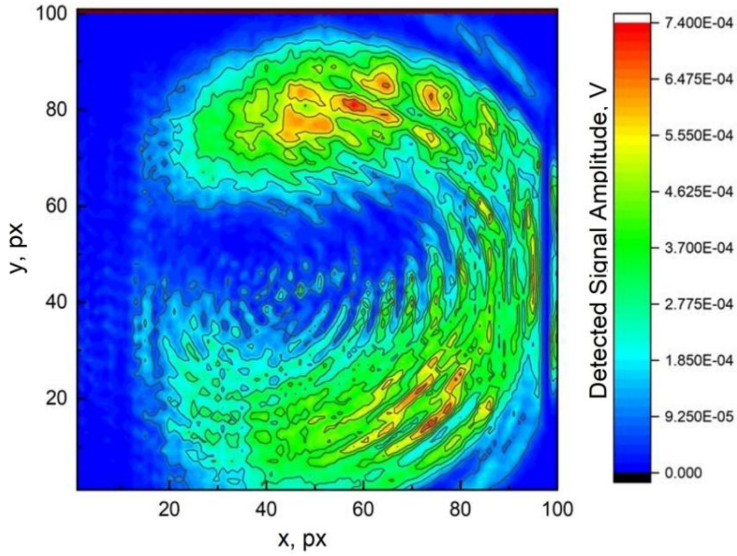

Fig. 25. Signal intensity map.

3.4. Mapping results for the TeraFET detector with an aperture

As shown in Figure 26, the signal intensity maps demonstrate the relationship between raw signal power and spatial precision in THz detection. Without an aperture (a), the incoming wave dispersed over a wide area upon reaching the single-pixel detector, resulting in a lack of concentration at the centre. Although the unfiltered beam achieves a peak amplitude of 0.3410 V, its energy distribution is spatially inconsistent and appears cluttered with reflections or distortions. Without an aperture, the detector captures a broader section of the wave. While this results in greater total power, it reduces the focus. It is worth noting that figures 25 and 26(a) show unfiltered signals that differ because these experiments were performed separately. The latter experiment had a slightly different, but more optimised, measurement setup.

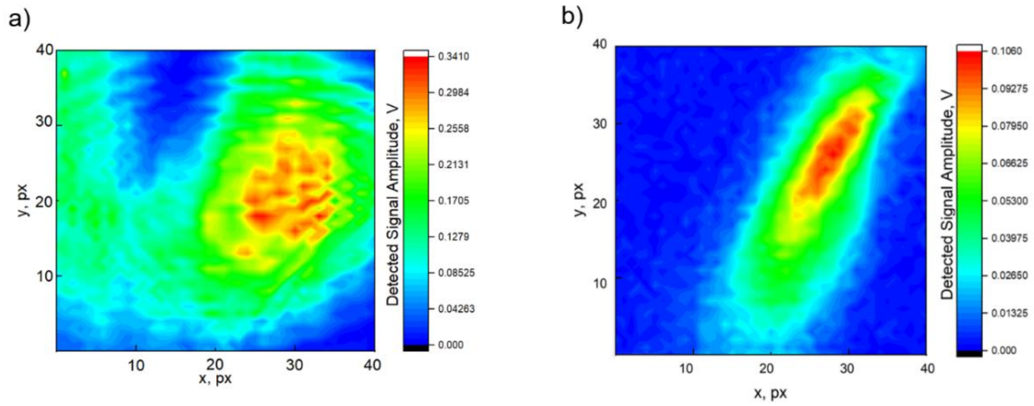

Fig. 26. Signal intensity map of a patch antenna detector: a) with no aperture; b) with 0.5 mm aperture (size of a single pixel is 0.3 mm by 0.3 mm).

Introducing a 0.5 mm aperture (b) causes the radiation to become tightly concentrated into an elliptical shape. The no-aperture configuration (a) has a peak amplitude of 0.3410 V, whereas the 0.5 mm aperture (b) peaks at 0.1060 V. Despite the absolute signal level being almost three times lower, the filtered beam provides a far more defined and consistent profile.

3.5. Angular dependence measurement results for the TeraFET detectors

In order to evaluate the spatial sensitivity and energy collection efficiency of the terahertz detectors, the angular beam profiles of the single-pixel detector and the 4x4 and 3x3 multi-pixel array detectors were measured. The results for the single-pixel detector were additionally compared to the simulation results.

3.5.1 Single-pixel detector

Figure 27 illustrates the angular dependence of the THz response, showing the directional sensitivity of a single-pixel detector across its two planes. This graph shows the average result of three measurements. The H-plane, represented by the black curve, features a wide radiation lobe extending from 55° to -55°, which enables a large detection field. The detector achieves its highest sensitivity in the H-plane, with a peak response of 4.5 μV, and has a relatively uniform and smooth profile at the centre.

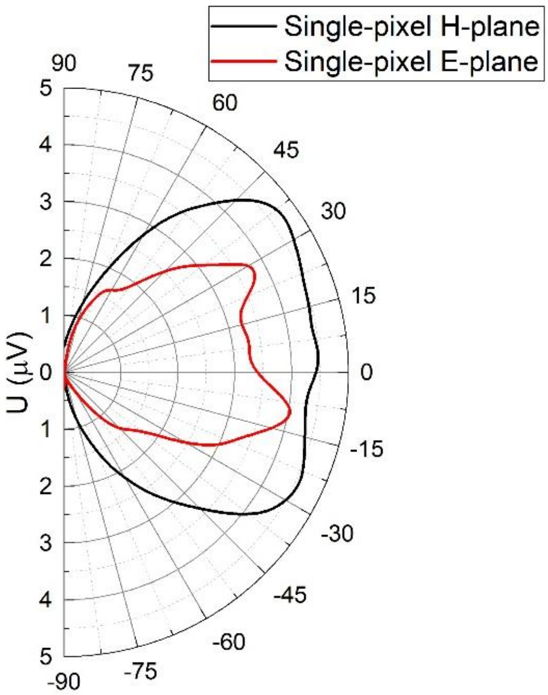

Fig. 27. Measured angular dependence of single-pixel TeraFET detector response voltage.

In contrast, the red curve (E-plane) is much narrower and has a more irregular shape. It is approximately 20° thinner than the H-plane and has two distinct peaks that reach a maximum of 4 μV, rather than one smooth curve. The directivity of the detector and its effective area have been calculated to be 6.2 dBi and 4.69×10^{-9} m², respectively.

When the experimental findings are compared with the simulation results, distinct differences in the shapes of the patterns and final values emerge. The simulated profiles for effective area and directivity are smooth and broad, centred on a single lobe at 0°. In contrast, the experimental results show greater narrowing and double peaks in the E plane. The simulation predicts lower directional performance. The simulated directivity peaks at 0 dBi on the central axis, whereas the experimental value is 6.2 dBi. Consequently, the simulated peak effective area is 9×10^{-10} m², which is approximately one-fifth of the 4.69×10^{-9} m² value calculated experimentally.

3.5.2 Multi-pixel detector with 4x4 array

Figure 28 shows that the 4x4 multi-pixel array has a much more concentrated response than the previous single-pixel design. The H-plane (black curve) spans from 35° to −35°, while the E-plane (red curve) is tighter still at 20° to −20°. This indicates that the multi-pixel array is far more efficient at focusing on radiation from a specific direction compared to single-pixel detector.

The peak signal strength for both planes is approximately 800 μV. Even after factoring in the module's amplification by a factor of 100, the 4x4 array still delivers a result at least twice as large as that of the single-pixel antenna. This confirms that the multi-pixel configuration not only narrows the field of view, but also significantly increases the total THz power captured.

Because of the improved focus, the directivity reaches 11.7 dBi, a significant jump from the 6.2 dBi of the single-pixel version. This gives an effective aperture of around 1.67×10^{-8} m². This capture area is over three times larger than that of the single-pixel detector, demonstrating that the array is far more effective at focusing and collecting energy along the main detection line.

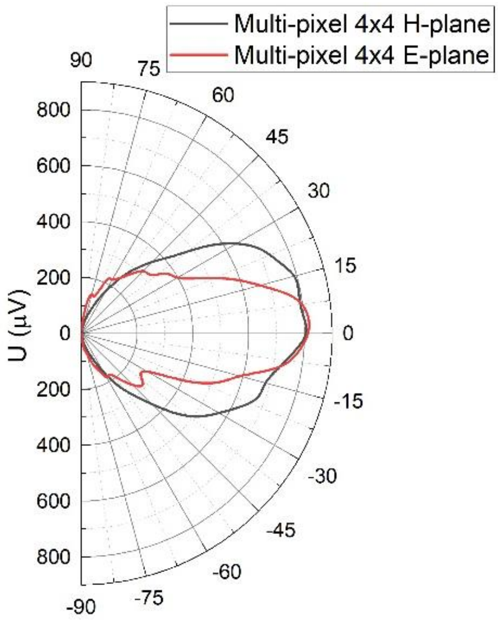

Fig. 28. Measured angular dependence of 4x4 multi-pixel TeraFET detector response voltage.

3.5.3 Multi-pixel detector with 3x3 array

Figure 29 illustrates the radiation pattern of the 3×3 multi-pixel array. The H-plane (black curve) has a lobe width ranging from 45° to -45°, whereas the E-plane (red curve) has a slightly tighter range of 35° to -35°. Unlike a single-pixel detector, this array has a more uniform shape and does not exhibit distinct double peaks, indicating that it captures the THz signal more consistently.

For this configuration, the peak signal voltage is approximately 100 μV. The E and H planes are not perfectly centred at 0° and are slightly offset from each other. It is likely that this offset is the result of a minor mechanical misalignment during the experimental setup. This could be due to the detector chip being mounted at a slight tilt or the rotary stage not being perfectly centred with the incoming THz beam.

Based on the observed beamwidth in Figure 29, the directivity is calculated to be approximately 9.4 dBi. At a frequency of 2.52 THz, this gives an effective aperture of about 9.8×10^{-9} m². While the 3×3 array provides approximately twice the effective capture area of a single-pixel detector, it is less directive than the larger 4×4 configuration, as expected given the smaller antenna footprint.

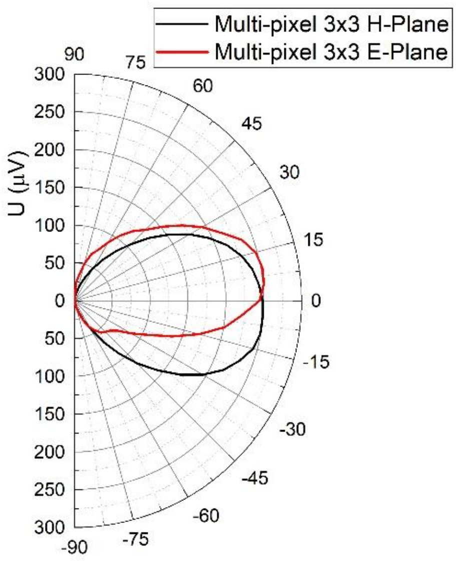

Fig. 29. Measured angular dependence of 3x3 multi-pixel TeraFET detector response voltage.

3.6. Comparison of the results

The normalised angular directivity plots in figure 30 clearly show an improvement in beam focusing and pattern symmetry when transitioning from a single-pixel detector to multi-pixel arrays. The single-pixel configuration exhibits a very broad H-plane lobe, while the E-plane response shows an asymmetric, double-peaked irregularity indicating non-uniform spatial sensitivity. By contrast, the multi-pixel configurations effectively eliminate these spatial distortions and reduce the angle of detection.

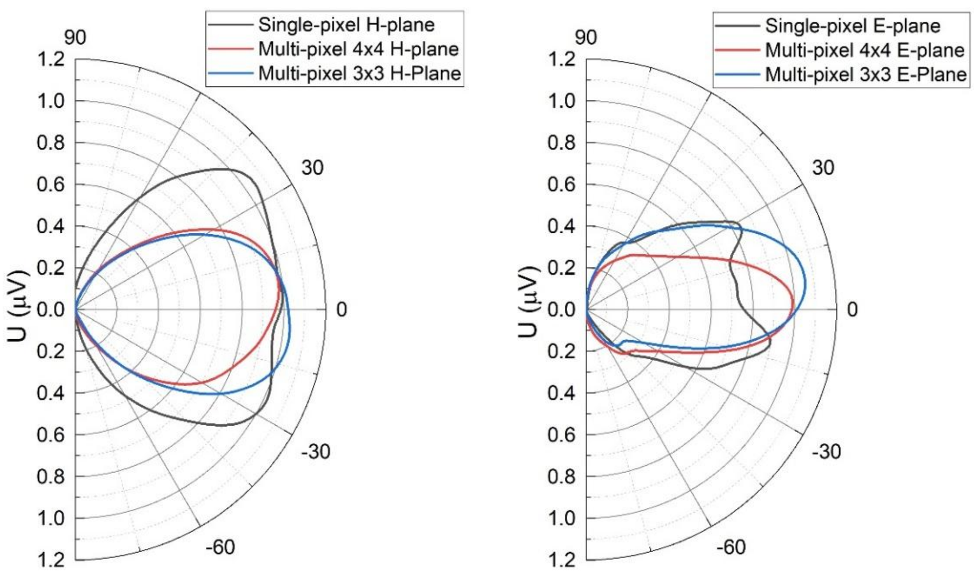

Fig. 30. Normalised angular dependence plots of different antenna configurations. H and E planes are separated.

A quantitative comparison of the measured parameters across the different patch configurations (presented in Table 3) shows that performance improves with increasing array size. The single-pixel antenna establishes the baseline, achieving a directivity (D) value of 6.2 dBi and an effective area (A_{eff}) of 4.69×10^{-9} m². Moving to the 3×3 multi-pixel array significantly improves these metrics, raising the directivity to 9.4 dBi, doubling the effective area to 9.8×10^{-9} m². The 4×4 multi-pixel array delivers the highest performance across all evaluated parameters, maximising the effective aperture at 1.67×10^{-8} m² and the directivity at 11.7 dBi. These results confirm that expanding the array matrix drastically improves the overall efficiency of signal collection and the sensitivity of the device.

Table 3. Comparison between the parameters of different antennas.

	Single-pixel antenna	Multi-pixel antenna 4x4	Multi-pixel antenna 3x3
U_{max}, μV	4.5	800	250
D, dBi	6.2	11.7	9.4
A_{eff}, m²	4.69×10^{-9}	1.67×10^{-8}	9.8×10^{-9}

CONCLUSIONS

1. Simulations of a patch antenna at 2.52 THz predict 0 dBi of directivity and an effective area of 9×10^{-10} m². However, single-pixel measurements in an experiment yielded a much higher directivity of 6.2 dBi, as well as an effective area that was five times larger at 4.69×10^{-9} m². This proves that simulations must include more defined antenna features.
2. Raster scan of a spatially-unfiltered THz beam reveals a doughnut-shaped profile, with a peak voltage of 0.3410 V. An aperture of 0.5 mm in the intermediate focal point improves the beam quality and results in an elliptical profile and a peak detected signal of 0.1060 V. This filtering assures the quality of angle-dependent experiments.
3. The single-pixel detector's H-plane lobe ranges from 55° to −55°, is smooth and peaks at 4.5 µV. The E-plane response is 20° narrower, irregularly double-peaked and reaches 4 µV. The values suggest a detection sensitivity that is broad but not uniform in terms of its spatial distribution.
4. The 4x4 array has a highly concentrated directional response, spanning from 35° to -35° in the H-plane, and 20° to -20° in the E-plane, delivering 800 µV across both planes. The 4x4 configuration efficiently increases detector's directivity.
5. The 3x3 array's uniform radiation pattern spans 45° to -45° in the H-plane and 35° to -35° in the E-plane, with a peak voltage of 100 µV. Unlike the single-pixel design, this array captures the THz signal consistently without distinct double peaks.
6. Evaluations show directivity and effective aperture values increase with increasing pixel count. The single-pixel detector offers 6.2 dBi and an effective aperture of $4.69\text{x}10^{-9}$ m², while the 3x3 array has higher directivity of 9.4 dBi and $9.8\text{x}10^{-9}$ m² effective aperture. The 4x4 array performs best, collecting energy directly with a directivity reaching 11.7 dBi and an effective aperture of $16.7\text{x}10^{-9}$ m².

OUTLOOK

The experimental results confirm that multi-pixel arrays significantly outperform single-pixel designs. They demonstrate clear improvements in terms of directivity and effective aperture. These findings provide a solid foundation for future research involving testing detectors tuned to a variety of resonant frequencies. To further characterise these devices, upcoming measurements will utilise multi-frequency laser sources to evaluate performance outside designated operating ranges. These tests will also measure the noise equivalent power, which will help to characterise the detector thoroughly and enable direct performance comparisons with other alternative detectors.

Furthermore, subsequent studies will involve a comparative analysis of single- and multi-pixel patch profiles to investigate the interaction of individual detector elements within an array. Understanding these interactions and potential interference is crucial for developing high-resolution detector matrices for quantum cascade laser (QCL) and other continuous-wave (CW) laser beam imaging applications. All of these research objectives are set to be addressed as part of my future PhD studies.

SOURCES

[1] R. Pant and L. Malviya, "THz antennas design, developments, challenges, and applications: A review," *Int. J. Commun. Syst.*, vol. 36, no. 8, p. e5474, 2023, doi: 10.1002/dac.5474.

[2] R. Köhler *et al.*, "Terahertz semiconductor-heterostructure laser," *Nature*, vol. 417, no. 6885, pp. 156–159, May 2002, doi: 10.1038/417156a.

[3] N. Akter, N. Pala, W. Knap, and M. Shur, "THz Plasma Field Effect Transistor Detectors," in *Fundamentals of Terahertz Devices and Applications*, John Wiley & Sons, Ltd, 2021, pp. 285–322. doi: 10.1002/9781119460749.ch8.

[4] James F. Buckwalter *et al.*, "Fundamental limits of high-efficiency silicon and compound semiconductor power amplifiers in 100-300 GHz bands," *ITU J. Future Evol. Technol.*, vol. 2, no. 7, pp. 39–50, Oct. 2021, doi: 10.52953/WOXT4388.

[5] S. Kumar, "Recent Progress in Terahertz Quantum Cascade Lasers," *IEEE J. Sel. Top. Quantum Electron.*, vol. 17, no. 1, pp. 38–47, Jan. 2011, doi: 10.1109/JSTQE.2010.2049735.

[6] P. S. Stefanova, J. M. Hammler, A. K. Klein, A. J. Gallant, and C. Balocco, "Polymer-based micro-golay cells for THz detection," in *2016 41st International Conference on Infrared, Millimeter, and Terahertz waves (IRMMW-THz)*, Sep. 2016, pp. 1–2. doi: 10.1109/IRMMW-THz.2016.7758964.

[7] F. Simoens, "THz Bolometer Detectors," in *Physics and Applications of Terahertz Radiation*, M. Perenzoni and D. J. Paul, Eds., Dordrecht: Springer Netherlands, 2014, pp. 35–75. doi: 10.1007/978-94-007-3837-9_2.

[8] R. Müller *et al.*, "Characterization of a Large-Area Pyroelectric Detector from 300 GHz to 30 THz," *J. Infrared Millim. Terahertz Waves*, vol. 36, no. 7, pp. 654–661, Jul. 2015, doi: 10.1007/s10762-015-0163-7.

[9] S. van Berkel *et al.*, "Wideband Modeling of CMOS Schottky Barrier Diode Detectors for THz Radiometry," *IEEE Trans. Terahertz Sci. Technol.*, vol. 11, no. 5, pp. 495–507, Sep. 2021, doi: 10.1109/TTHZ.2021.3085137.

[10] W. Knap *et al.*, "Field Effect Transistors for Terahertz Detection: Physics and First Imaging Applications," *J. Infrared Millim. Terahertz Waves*, vol. 30, no. 12, pp. 1319–1337, Dec. 2009, doi: 10.1007/s10762-009-9564-9.

[11] N. T. Yardimci and M. Jarrahi, “Nanostructure-Enhanced Photoconductive Terahertz Emission and Detection,” *Small*, vol. 14, no. 44, p. 1802437, 2018, doi: 10.1002/smll.201802437.

[12] Z. Bielecki, J. Mikolajczyk, and J. Wojtas, “A Review of Thermal Detectors of THz Radiation Operated at Room Temperature,” *Sensors*, vol. 24, no. 21, p. 6784, Jan. 2024, doi: 10.3390/s24216784.

[13] “TYDEX Golay Detectors.” Accessed: Apr. 03, 2026. [Online]. Available: https://www.tydexoptics.com/products/thz_devices/golay_cell/

[14] F. Sizov and A. Rogalski, “THz detectors,” *Prog. Quantum Electron.*, vol. 34, no. 5, pp. 278–347, Sep. 2010, doi: 10.1016/j.pquantelec.2010.06.002.

[15] “High Sensitive.” Accessed: Apr. 03, 2026. [Online]. Available: https://www.pyrosensor.de/High-Sensitive-922643.html

[16] E. N. Grossman and A. J. Miller, “Active millimeter-wave imaging for concealed weapons detection,” presented at the AeroSense 2003, R. Appleby, D. A. Wikner, R. Trebits, and J. L. Kurtz, Eds., Orlando, FL, Aug. 2003, p. 62. doi: 10.1117/12.488198.

[17] T.-L. Hwang, S. E. Schwarz, and D. B. Rutledge, “Microbolometers for infrared detection,” *Appl. Phys. Lett.*, vol. 34, no. 11, pp. 773–776, Jun. 1979, doi: 10.1063/1.90669.

[18] “Ambient temperature or moderately cooled semiconductor hot electron bolometer for mm and sub-mm regions | Opto-Electronics Review | Springer Nature Link.” Accessed: Apr. 03, 2026. [Online]. Available: https://link.springer.com/article/10.2478/s11772-008-0003-6

[19] V. N. Dobrovolsky, F. F. Sizov, Y. E. Kamenev, and A. B. Smirnov, “Ambient temperature or moderately cooled semiconductor hot electron bolometer for mm and sub-mm regions,” *Opto-Electron. Rev.*, vol. 16, no. 2, pp. 172–178, Jun. 2008, doi: 10.2478/s11772-008-0003-6.

[20] “InSb Hot Electron Bolometer,” QMC Instruments. Accessed: Apr. 03, 2026. [Online]. Available: https://www.qmcinstruments.co.uk/insb-hot-electron-bolometer/

[21] I. Mehdi, J. V. Siles, C. Lee, and E. Schlecht, “THz Diode Technology: Status, Prospects, and Applications,” *Proc. IEEE*, vol. 105, no. 6, pp. 990–1007, Jun. 2017, doi: 10.1109/JPROC.2017.2650235.

[22] R. Tauk *et al.*, “Plasma wave detection of terahertz radiation by silicon field effects transistors: Responsivity and noise equivalent power,” *Appl. Phys. Lett.*, vol. 89, no. 25, p. 253511, Dec. 2006, doi: 10.1063/1.2410215.

[23] J. Holstein *et al.*, "8×8 Patch-Antenna-Coupled TeraFET Detector Array for Terahertz Quantum-Cascade-Laser Applications," *IEEE Trans. Terahertz Sci. Technol.*, vol. 14, no. 6, pp. 799–807, Nov. 2024, doi: 10.1109/TTHZ.2024.3438429.

[24] A. Krysl *et al.*, "Si Superstrate Lenses on Patch-Antenna- Coupled TeraFETs: NEP Optimization and Frequency Fine-Tuning," *IEEE Sens. J.*, vol. 24, no. 21, pp. 33872–33880, Nov. 2024, doi: 10.1109/JSEN.2024.3445140.

[25] R. Yadav *et al.*, "GaAs-based antenna-coupled field effect transistors as direct THz detectors across a wide frequency range from 0.2 to 29.8 THz," *Opt. Express*, vol. 32, no. 24, pp. 43407–43416, Nov. 2024, doi: 10.1364/OE.534393.

[26] R. Yadav *et al.*, "GaAs-based antenna-coupled field effect transistors as direct THz detectors across a wide frequency range from 0.2 to 29.8 THz," *Opt. Express*, vol. 32, no. 24, pp. 43407–43416, Nov. 2024, doi: 10.1364/OE.534393.

[27] D. Dragoman and M. Dragoman, "Terahertz fields and applications," *Prog. Quantum Electron.*, vol. 28, no. 1, pp. 1–66, Jan. 2004, doi: 10.1016/S0079-6727(03)00058-2.

[28] L. G. Yamamoto, "Risks and Management of Radiation Exposure," *Pediatr. Emerg. Care*, vol. 29, no. 9, p. 1016, Sep. 2013, doi: 10.1097/PEC.0b013e3182a380b8.

[29] P. H. Siegel, "THz Technology: An Overview," *Int. J. High Speed Electron. Syst.*, vol. 13, no. 02, pp. 351–394, Jun. 2003, doi: 10.1142/S0129156403001776.

[30] Y. Zhang and M. S. Shur, "TeraFET terahertz detectors with spatially non-uniform gate capacitances," *Appl. Phys. Lett.*, vol. 119, no. 16, p. 161104, Oct. 2021, doi: 10.1063/5.0069072.

[31] G. Gopal, M. Kumawat, and T. Varma, "Recent Advancement in TFET-Based Biosensor Addressing Technique and Outcome: A Review," in *Biosensors: Developments, Challenges and Perspectives*, R. Mathew and J. Ajayan, Eds., Singapore: Springer Nature, 2024, pp. 119–145. doi: 10.1007/978-981-97-3048-3_7.

[32] R. Bala and A. Marwaha, "Characterization of graphene for performance enhancement of patch antenna in THz region," *Optik*, vol. 127, no. 4, pp. 2089–2093, Feb. 2016, doi: 10.1016/j.ijleo.2015.11.029.

[33] Y. He, Y. Chen, L. Zhang, S.-W. Wong, and Z. N. Chen, "An overview of terahertz antennas," *China Commun.*, vol. 17, no. 7, pp. 124–165, Jul. 2020, doi: 10.23919/J.CC.2020.07.011.

[34] A. S. Mohammed, "Microstrip Patch Antenna: A Review and the Current State of the Art," *Control Syst.*, vol. 11, 2019.

[35] S.-L. S. Yang, A. A. Kishk, and K.-F. Lee, “Frequency Reconfigurable U-Slot Microstrip Patch Antenna,” *IEEE Antennas Wirel. Propag. Lett.*, vol. 7, pp. 127–129, 2008, doi: 10.1109/LAWP.2008.921330.

[36] M. Kamran Shereen, M. I. Khattak, and G. Witjaksono, “A brief review of frequency, radiation pattern, polarization, and compound reconfigurable antennas for 5G applications,” *J. Comput. Electron.*, vol. 18, no. 3, pp. 1065–1102, Sep. 2019, doi: 10.1007/s10825-019-01336-0.

[37] J. W. Jayasinghe, J. Anguera, and D. N. Uduwawala, “A HIGH-DIRECTIVITY MICROSTRIP PATCH ANTENNA DESIGN BY USING GENETIC ALGORITHM OPTIMIZATION,” *Prog. Electromagn. Res. C*, vol. 37, pp. 131–144, 2013, doi: 10.2528/PIERC13010805.

[38] A. Katyal and A. Basu, “Compact and Broadband Stacked Microstrip Patch Antenna for Target Scanning Applications,” *IEEE Antennas Wirel. Propag. Lett.*, vol. 16, pp. 381–384, 2017, doi: 10.1109/LAWP.2016.2578723.

[39] A. Foroozesh and L. Shafai, “Investigation Into the Effects of the Patch-Type FSS Superstrate on the High-Gain Cavity Resonance Antenna Design,” *IEEE Trans. Antennas Propag.*, vol. 58, no. 2, pp. 258–270, Feb. 2010, doi: 10.1109/TAP.2009.2037702.

[40] A. Bakhtiari, “Investigation of Enhanced Gain Miniaturized Patch Antenna Using Near Zero Index Metamaterial Structure Characteristics,” *IETE J. Res.*, vol. 68, no. 2, pp. 1312–1319, Mar. 2022, doi: 10.1080/03772063.2019.1644973.

[41] J. Lee and S. Nam, “Effective Area of a Receiving Antenna in a Lossy Medium,” *IEEE Trans. Antennas Propag.*, vol. 57, no. 6, pp. 1843–1845, Jun. 2009, doi: 10.1109/TAP.2009.2019988.

[42] H. Lan and X. Wang, “The theoretical analysis of the THz of the CO2 laser pumped CH3OH,” in *International Symposium on Photonics and Optoelectronics 2014*, SPIE, Aug. 2014, pp. 238–242. doi: 10.1117/12.2068270.

[43] F. Fei, W. Jing, T. Zhaoshuo, Z. Yanchao, F. Shiyou, and W. Qi, “Theoretical and Experimental studies on CH3OH THz Laser Pumped by Pulse Carbon Dioxide Laser,” *J. Phys. Conf. Ser.*, vol. 276, no. 1, p. 012203, Feb. 2011, doi: 10.1088/1742-6596/276/1/012203.

[44] C. A. Balanis, *Antenna theory: analysis and design$nElektronische Ressource*, 3. ed. Hoboken, N.J: Wiley-Interscience, 2005.

[45] “From Array Theory to Shared Aperture Arrays.” Accessed: May 18, 2026. [Online]. Available: https://www.sciencedirect.com/science/chapter/monograph/pii/B9780122629426500044

[46] A. Krysl *et al.*, “Si Superstrate Lenses on Patch-Antenna-Coupled TeraFETs: NEP Optimization and Frequency Fine-Tuning,” Apr. 11, 2024, *arXiv*: arXiv:2404.07715. doi: 10.48550/arXiv.2404.07715.

[47] L. A. Sterczewski, M. P. Grzelczak, and E. F. Plinski, “Terahertz antenna electronic chopper,” *Rev. Sci. Instrum.*, vol. 87, no. 1, p. 014702, Jan. 2016, doi: 10.1063/1.4939461.

[48] Y. Nemirovsky, I. Brouk, and C. G. Jakobson, “1/f noise in CMOS transistors for analog applications,” *IEEE Trans. Electron Devices*, vol. 48, no. 5, pp. 921–927, May 2001, doi: 10.1109/16.918240.

[49] L. Minkevičius *et al.*, “Titanium-Based Microbolometers: Control of Spatial Profile of Terahertz Emission in Weak Power Sources,” *Appl. Sci.*, vol. 10, no. 10, p. 3400, Jan. 2020, doi: 10.3390/app10103400.

SUMMARY

To bridge the terahertz gap, room-temperature patch-antenna-coupled TeraFET detectors were developed using a 65-nm CMOS process optimized for 2.52 THz operation. The methodology progressed from ADS numerical antenna modelling and LTspice electrical simulation. A highly stable OPA858/OPA211 multi-stage amplifier was implemented to minimise room-temperature 1/f noise. After custom PCB soldering, precise microscopic chip alignment and wire bonding, the sensors were integrated into a 30 mm cage measurement system. Spatial and angular characterisation of single-pixel, 3×3 and 4×4 array THz antennas utilised a CO_2-pumped FIR laser, an optical chopper and a DSP lock-in amplifier. To map profiles, an automated X-Y translation stage was used.

Experimental characterisation yielded vital performance metrics that verified the design. IV analysis revealed typical gate-modulated resistance, peaking in responsivity at 0.6 V (1,000 Ω). The single-pixel detector significantly outperformed the simulations, achieving a directivity of 6.2 dBi and an effective area of 4.69×10^{-9} m² – five times larger than predicted. Spatial mapping revealed that a 0.5 mm aperture was necessary to transform an unfiltered, doughnut-shaped beam profile (0.3410 V) into a focused, elliptical shape (0.1060 V) and eliminate background reflections effectively. Multi-pixel arrays drastically improved signal uniformity by eliminating the irregular E-plane double peaks of the single pixel. Performance scaled efficiently with array size, establishing the 4×4 configuration as the optimal design through maximising energy collection with elevated 11.7 dBi directivity, an expanded 1.67×10^{-8} m² effective area.

SANTRAUKA

Siekiant užpildyti terahercų spragą, buvo sukurti kambario temperatūroje veikiantys, su patch antena sujungti „TeraFET“ detektoriai, pagaminti naudojant 65 nm CMOS technologiją, optimizuotą darbui 2,52 THz dažniu. Metodika buvo plėtojama remiantis ADS skaitmeniniu antenų modeliavimu ir LTspice elektrine simuliacija. Siekiant sumažinti kambario temperatūroje susidarančius 1/f triukšmus, buvo įdiegtas itin stabilus daugiapakopis stiprintuvas OPA858/OPA211. Po individualaus PCB litavimo, tikslaus mikroskopinio lustų išlyginimo ir laidų privirinimo, jutikliai buvo integruoti į 30 mm korpuso matavimo sistemą. Vieno pikselio, 3×3 ir 4×4 matricos terahercinių antenų erdvinėms ir kampinėms charakteristikoms nustatyti buvo naudojamas su CO_2 pumpuojamas FIR lazeris, optinis čoperis ir DSP lock-in stiprintuvas. Profiliams nubraižyti buvo naudojamas automatinis X-Y poslinkio stendas.

Eksperimentinis charakterizavimas leido gauti esminius veikimo rodiklius, patvirtinančius dizainą. IV analizė parodė tipišką užtūros moduliuotą varžą, kurios jautrumas pasiekė maksimumą esant 0,6 V (1 000 Ω). Vieno pikselio detektorius gerokai pranoko modeliavimo rezultatus, pasiekdamas 6,2 dBi kryptingumą ir $4{,}69\times10^{-9}$ m² efektyvųjį plotą – penkis kartus didesnį nei buvo prognozuota. Erdvinis profiliavimas parodė, kad reikėjo 0,5 mm apertūros, norint suspausti nefiltruotą, žiedo formos spindulio profilį (0,3410 V) į fokusuotą elipsės formą (0,1060 V), veiksmingai pašalinant foninius atspindžius. Kelių pikselių matricos detektoriai žymiai pagerino signalo vienodumą, pašalindamos vieno pikselio nereguliarius E-plokštumos dvigubas viršūnes. Našumas efektyviai didėjo kartu su matricos dydžiu, o 4×4 konfigūracija tapo optimaliausiu detektoriumi, maksimaliai padidinančiu energijos surinkimą su 11,7 dBi kryptingumu, $1{,}67\times10^{-8}$ m² efektyviuoju plotu.